ARTICLES

Journal of Semiconductors
(2024) 45, 032703
doi: 10.1088/1674-4926/45/3/032703

Visible-to-near-infrared photodetectors based on $SnS/SnSe_2$ and $SnSe/SnSe_2$ p–n heterostructures with a fast response speed and high normalized detectivity

Xinfa Zhu[1, ‡], Weishuai Duan[1, ‡], Xiancheng Meng[1], Xiyu Jia[1], Yonghui Zhang[1], Pengyu Zhou[2, †], Mengjun Wang[1], Hongxing Zheng[1], and Chao Fan[1, †]

[1]School of Electronic and Information Engineering, Hebei University of Technology, Tianjin 300401, China

[2]School of Science, Northeast Electric Power University, Jilin 132012, China

Abstract: The emergent two-dimensional (2D) material, tin diselenide ($SnSe_2$), has garnered significant consideration for its potential in image capturing systems, optical communication, and optoelectronic memory. Nevertheless, $SnSe_2$-based photodetection faces obstacles, including slow response speed and low normalized detectivity. In this work, photodetectors based on $SnS/SnSe_2$ and $SnSe/SnSe_2$ p–n heterostructures have been implemented through a polydimethylsiloxane (PDMS)–assisted transfer method. These photodetectors demonstrate broad-spectrum photoresponse within the 405 to 850 nm wavelength range. The photodetector based on the $SnS/SnSe_2$ heterostructure exhibits a significant responsivity of 4.99×10^3 $A{\cdot}W^{-1}$, normalized detectivity of 5.80×10^{12} $cm{\cdot}Hz^{1/2}{\cdot}W^{-1}$, and fast response time of 3.13 ms, respectively, owing to the built-in electric field. Meanwhile, the highest values of responsivity, normalized detectivity, and response time for the photodetector based on the $SnSe/SnSe_2$ heterostructure are 5.91×10^3 $A{\cdot}W^{-1}$, 7.03×10^{12} $cm{\cdot}Hz^{1/2}{\cdot}W^{-1}$, and 4.74 ms, respectively. And their photodetection performances transcend those of photodetectors based on individual $SnSe_2$, SnS, SnSe, and other commonly used 2D materials. Our work has demonstrated an effective strategy to improve the performance of $SnSe_2$-based photodetectors and paves the way for their future commercialization.

Key words: two-dimensional materials; tin diselenide; heterostructures; broad-spectrum photodetectors

Citation: X F Zhu, W S Duan, X C Meng, X Y Jia, Y H Zhang, P Y Zhou, M J Wang, H X Zheng, and C Fan, Visible-to-near-infrared photodetectors based on $SnS/SnSe_2$ and $SnSe/SnSe_2$ p–n heterostructures with a fast response speed and high normalized detectivity[J]. *J. Semicond.*, 2024, 45(3), 032703. https://doi.org/10.1088/1674-4926/45/3/032703

1. Introduction

Since 2004, significant attention has been directed towards two-dimensional (2D) materials such as graphene (GP), black phosphorus (BP), and molybdenum disulfide (MoS_2), due to their extraordinary atomic-scale thickness, remarkable mechanical strength, and robust light–matter interaction[1–3]. As a nascent member of 2D materials, tin diselenide ($SnSe_2$) is an instinct n-type Ⅳ–Ⅵ semiconductor with a Se–Sn–Se sandwich-layered structure and a bandgap of ~1 eV[4]. Furthermore, with its exceptional qualities of high carrier mobility (462 $cm^2/(V{\cdot}s)$)[5], absorption coefficient (7.25×10^5 cm^{-1})[6], environmental friendliness[7], and chemical stability[8], $SnSe_2$ is a superior material for high-sensitivity and low-consumption photodetectors, which can be widely used in image acquisition[9], information communication[10], and photo-electronic memory[11]. For example, Chen *et al*. fabricated a $SnSe_2$-based photodetector via low-temperature molecular beam epitaxy, which demonstrated a normalized detectivity of 6.09×10^9 $cm{\cdot}Hz^{1/2}{\cdot}W^{-1}$ under 532 nm illumination[12]. Zhai *et al*. fabricated a $SnSe_2$-based photodetector using chemical vapor deposition, which exhibited a normalized detectivity of 1.01×10^{10} $cm{\cdot}Hz^{1/2}{\cdot}W^{-1}$ and a response time of 14.5 ms under 530 nm illumination[13].

However, $SnSe_2$-based photodetectors suffer from drawbacks such as large dark current, slow response time, and low normalized detectivity, which limits their potential for commercial application. To surmount these challenges and enhance the photodetection performance of $SnSe_2$-based photodetectors, stacking van der Waals heterostructures has been established as an effective strategy. This is due to the unique properties of van der Waals heterostructures, including the absence of dangling surfaces, strong interlayer coupling, and ultrafast charge transfer[14, 15]. For example, Zhou *et al*. successfully achieved a photodetector based on a $SnSe_2/MoS_2$ heterostructure. The photodetector exhibited a normalized detectivity of 9.3×10^{10} $cm{\cdot}Hz^{1/2}{\cdot}W^{-1}$ under 500 nm illumination, which was one order of magnitude higher than that of the photodetector based on the individual $SnSe_2$ and MoS_2 components[16]. Zheng *et al*. reported a photodetector based on an $In_2Se_3/SnSe_2$ heterostructure that outperformed the device based on the individual components by one order of magnitude, achieving a high normalized detectivity of 8.8×10^{11} $cm{\cdot}Hz^{1/2}{\cdot}W^{-1}$ under 477 nm illumination[17]. However, more efforts should be devoted to elucidating the underlying mechanisms of $SnSe_2$-based heterostructures.

Xinfa Zhu and Weishuai Duan contributed equally to this work and should be considered as co-first authors.

Correspondence to: P Y Zhou, 20162715@neepu.edu.cn; C Fan, fanch@hebut.edu.cn

Received 7 NOVEMBER 2023; Revised 22 NOVEMBER 2023.

As members of the Ⅳ–Ⅵ compounds, tin mono-sulfide (SnS) and tin mono-selenide (SnSe) exhibit inherent p–type semiconductivity with an orthorhombic Sn–S (Se) layered structure[18, 19]. Given their common metallic atoms, it is both feasible and convenient to realize p–n heterostructures of SnS/$SnSe_2$ and SnSe/$SnSe_2$. In this work, photodetectors based on SnS/$SnSe_2$ and SnSe/$SnSe_2$ p–n heterostructures (denoted as the SnS/$SnSe_2$ and SnSe/$SnSe_2$ photodetectors) were constructed by a polydimethylsiloxane (PDMS)-assisted dry-transfer method, and then investigated. Our results demonstrate that these photodetectors manifested superior photodetection performance, encompassing enhanced responsivity, normalized detectivity, and response speed in comparison to photodetectors based on individual $SnSe_2$, SnS, and SnSe components. This work expands the research scope of $SnSe_2$-based photodetectors and holds great promise for future optoelectronic applications.

2. Experimental

2.1. Growth and characterization of materials

Single crystals of $SnSe_2$, SnS, and SnSe were prepared by a chemical vapor transport (CVT) technique. The purity of precursors (Se, S, and Sn powders) was 99.99%, and they were purchased from Aladdin (Shanghai, CN). For $SnSe_2$, Sn and Se powders were hermetically vacuum-sealed in a quartz tube under a vacuum of 10^{-5} Torr with a stoichiometric ratio of 1 ∶ 2. The precursors were heated by gradient heating: initially, the temperature was heated to 610 ℃, and held for 24 h. In the next step, the temperature was decreased to 600 ℃ and held for 120 h. Finally, they were cooled to room temperature. As to SnS, Sn and S powders were also vacuum-sealed in a quartz tube under a vacuum of 10^{-5} Torr with a stoichiometric ratio of 1 ∶ 1. The precursors were subjected to gradient heating: initially, the temperature was raised to 950 ℃ and held for 24 h. In the subsequent step, the temperature was lowered to 850 ℃ and held for 120 h. Finally, they were cooled to room temperature. For SnSe, Sn and Se powders were hermetically sealed with a stoichiometric ratio of 1 ∶ 1. The precursors were subjected to gradient heating: initially, the temperature was raised to 900 ℃ and maintained for 24 h. In the subsequent step, the temperature was cooled to 800 ℃ and held for 120 h. Finally, the precursors were cooled down to room temperature.

The composition and phase of the crystals were probed using an X–ray diffractometer (XRD, Smartlab, Rigaku) with Cu Kα radiation of λ = 0.15406 nm. The elemental composition and valence of the samples were assessed using an X–ray photoelectron spectroscope with an excitation source of 532 nm (XPS, Escalab 250 Xi, Thermo Fisher). The Raman spectrometer (InVia, Renishaw) was utilized to characterize the vibrational mode and material identification under the excitation source of 532 nm. The surface morphology was evaluated using an atomic force microscope (AFM, Ntegra Spectra, NT–MDT) in tapping mode and an optical microscope (OM, Olympus BX51M).

2.2. Preparation and measurement of devices

Photodetectors based on SnS/$SnSe_2$ and SnSe/$SnSe_2$ heterostructures were stacked by a polydimethylsiloxane (PDMS)-assisted dry-transfer method, and Au electrodes were fabricated on substrates via means of lithography and electron beam evaporation. In the case of SnS/$SnSe_2$, $SnSe_2$ and SnS thin films were exfoliated from their single crystals and transferred onto the substrate using PDMS films. Subsequently, $SnSe_2$ thin films were stacked onto the SnS thin films with the assistance of an optical microscope. For SnSe/$SnSe_2$, $SnSe_2$ and SnSe thin films were exfoliated from their single crystals, and SnSe thin films were transferred onto the substrate using PDMS films. Subsequently, $SnSe_2$ thin films were stacked onto the SnSe thin films with the assistance of an optical microscope. The heterostructures were then transferred onto the substrate.

The photodetection performance of the photodetectors was assessed by a self-assembled photoelectric measurement system, which comprised a probe station (PW–600, Advanced), a semiconductor device analyzer (B1500A, Keysight), a waveform generator (33500B, Keysight), and four semiconductor lasers (with a wavelength of 405, 532, 650, and 850 nm and a spot diameter of 200 μm). The power density of the lasers was ascertained by a handheld laser power and energy meter (Nova Ⅱ, Ophir).

3. Results and discussion

Crystals of $SnSe_2$, SnS, and SnSe were synthesized via CVT, and their phase structures were probed by XRD. Fig. 1(a) shows XRD patterns of the as-grown crystals. The diffraction peaks are consistent with the standard cards of hexagonal-$SnSe_2$ (JCPDS No.23-0602), orthorhombic-SnS (JCPDS No.39-0354), and orthorhombic-SnSe (JCPDS No.48-1224)[20–22]. No phases related to other impurities like SnO and SnO_2 were detected. The strongest peaks corresponding to the (001), (003), (004), and (005) planes of $SnSe_2$ indicate the *c*-axis preferred orientation. The (111) plane preferred orientation of SnS and SnSe, on the other hand, is indicated by the strongest peaks at 31.97° and 30.89°, respectively. The inset of Fig. 1(a) shows the corresponding optical microscopy images and all the crystals showed gray-black metallic lusters with a lateral size of >4 mm.

In order to verify their chemical compositions and chemical states, XPS measurements were conducted. Fig. 1(b) illustrates the XPS spectra of the $SnSe_2$, SnS, and SnSe crystals. For $SnSe_2$, four peaks located at 52.5, 53.5, 485.3, and 494.6 eV are ascribed to the Se3$d_{5/2}$, Se3$d_{3/2}$, Sn3$d_{5/2}$, and Sn3$d_{3/2}$ orbitals of $SnSe_2$, indicating the presence of the Se^{2-} and Sn^{4+} states[23]. The atomic ratio of Sn to Se was determined to be 1 : 2.03 ($SnSe_{2.03}$). For SnS and SnSe, two peaks located at 493.3 and 484.91 eV are attributed to the Sn3$d_{5/2}$ and Sn3$d_{3/2}$ orbitals of the Sn^{2+} state. Four peaks located at 161.3, 160.4, 54.7, and 53.1 eV correspond to the S2$p_{1/2}$, S2$p_{3/2}$, Se3$d_{5/2}$, and Se3$d_{3/2}$ orbitals of SnS and SnSe, respectively[24, 25]. The atomic ratios of Sn to S and Sn to Se were determined to be 1 : 1.08 ($SnS_{1.08}$) and 1 : 1.02 ($SnSe_{1.02}$), respectively.

Following the fabrication of the SnS/$SnSe_2$ and SnSe/$SnSe_2$ photodetectors through a polydimethylsiloxane (PDMS)–assisted dry–transfer technique, the two types of heterostructures were characterized *in–situ* (Fig. S1 (a)). The surface morphologies of the heterostructures were detected by AFM. As illustrated in Fig. 2(a), the SnS/$SnSe_2$ and SnSe/$SnSe_2$ heterostructures possess clean surfaces devoid of any impurities, undulations, or bubbles. The height profiles of the

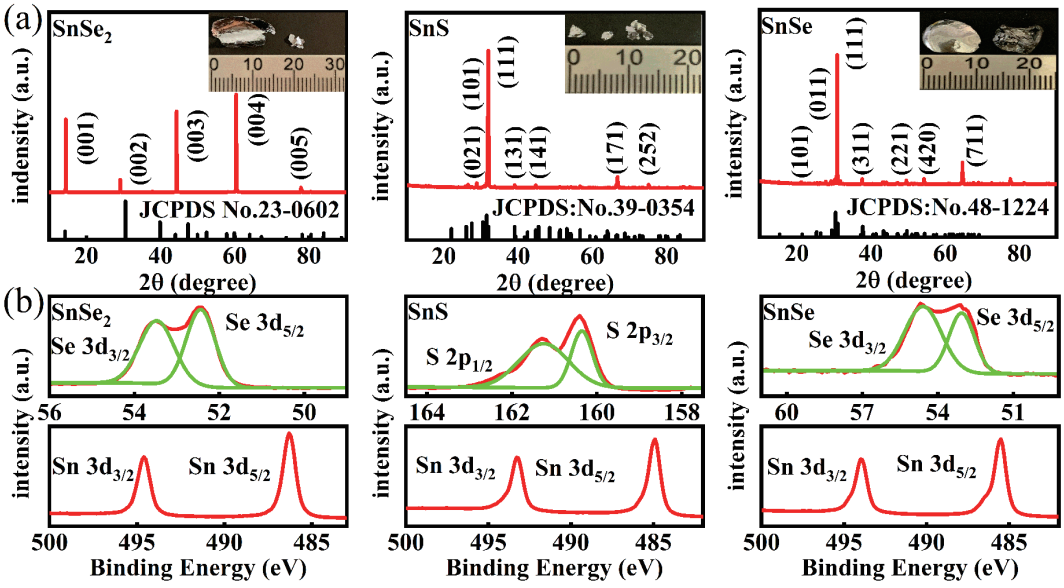

Fig. 1. (Color online) (a) XRD patterns of the $SnSe_2$, SnS, and SnSe crystals. The insets are the corresponding optical microscopy images. (b) XPS spectra of the SnS, SnS, and SnSe crystals.

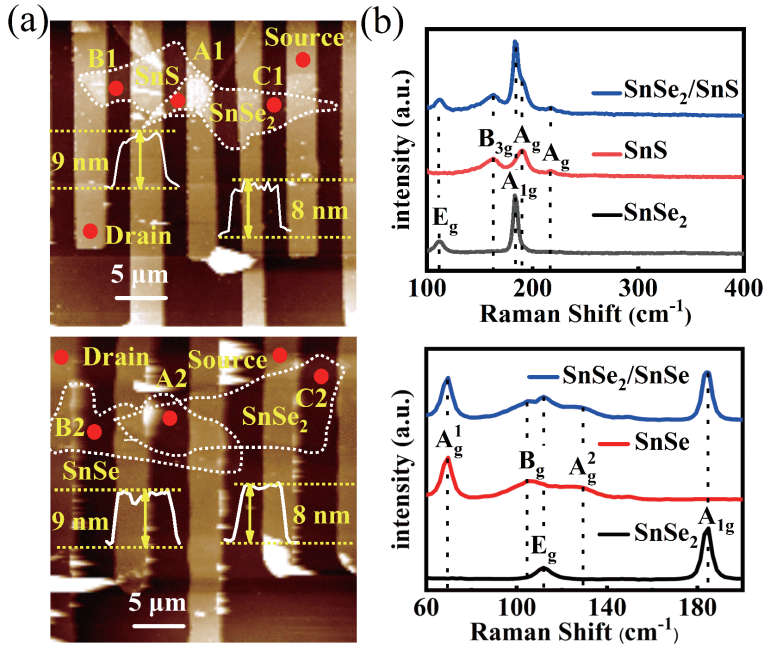

Fig. 2. (Color online) (a) AFM results of the $SnS/SnSe_2$ and $SnSe/SnSe_2$ heterostructures. The insets are the corresponding height profile. (b) Raman spectra of the $SnS/SnSe_2$ and $SnSe/SnSe_2$ heterostructures.

$SnS/SnSe_2$ heterostructure reveal that the individual SnS and $SnSe_2$ thin layers are 8 nm (~15 layers) and 9 nm (~12 layers) in thickness, respectively[4, 18]. Meanwhile, the thicknesses of the SnSe and $SnSe_2$ in the $SnSe/SnSe_2$ heterostructure were determined to be 9 nm (~15 layers) and 8 nm (~12 layers), respectively[19].

Fig. 2(b) presents the Raman spectra of the $SnS/SnSe_2$ and $SnSe/SnSe_2$ heterostructures. And the Raman spectrum of each heterostructure can be regarded as the combination of the individual Raman spectra of SnS, SnSe, and $SnSe_2$, thereby confirming the successful formation of the heterostructures. In the Raman spectrum of the $SnS/SnSe_2$ heterostructure, five peaks were observed (position A1). Two of these peaks located at 109.7 and 184.6 cm^{-1} were attributed to the E_g and A_{1g} vibration modes of $SnSe_2$ (position C1), while the remaining three peaks at 161.2, 188.4, and 216.1 cm^{-1} were attributed to the B_{3g} and A_g vibration modes of SnS (position B1)[26, 27]. Similarly, peaks corresponding to the E_g and A_{1g} vibration modes of $SnSe_2$ (position C2), as well as the A_g^1, B_g, and A_g^2 vibration modes of SnSe (position B2) can be found in the Raman spectrum of the $SnSe/SnSe_2$ heterostructure (position A2)[19].

The electrical characteristics of the $SnS/SnSe_2$ and $SnSe/SnSe_2$ photodetectors were probed by employing Au layers (50 nm) as the source and drain electrodes, while a heavily p–doped Si layer was utilized as the back gate. The output characteristics of the photodetectors were acquired by sweeping the source–drain voltage from −5 to 5 V and varying the gate–source voltage V_{gs} from −50 to 50 V, as illuminated in Figs. 3(a) and 3(b). The p–n junction demonstrated

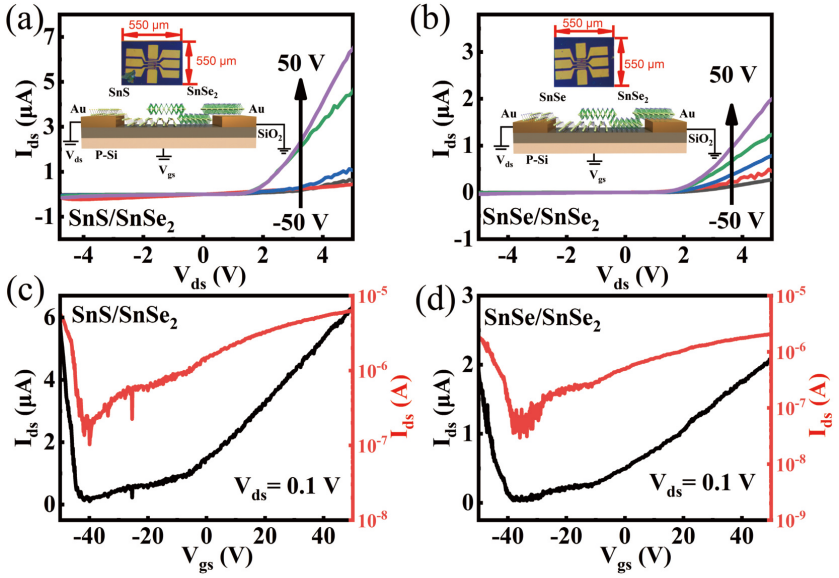

Fig. 3. (Color online) (a) and (b) Output characteristics of the $SnS/SnSe_2$ and $SnSe/SnSe_2$ photodetectors. The insets: the schematic diagrams and the optical images of the photodetectors. (c) and (d) Transfer characteristics on linear (left) and semi-logarithmic (right) scales of the $SnS/SnSe_2$ and $SnSe/SnSe_2$ photodetectors.

remarkable gate-tunable rectification behaviors, with rectification ratios of 55 and 110 observed at V_{gs} = 25 V for the $SnS/SnSe_2$ and $SnSe/SnSe_2$ photodetectors, respectively[28]. Figs. 3(c) and 3(d) depict the transfer curves of the photodetectors, which exhibited bipolar behavior attributed to the p-type SnS (SnSe) and n-type $SnSe_2$. Notably, for the $SnS/SnSe_2$ photodetector, the charge transport was dominated by holes when $V_{gs} < -42.55$ V, whereas electrons governed the charge transport when $V_{gs} > -42.55$ V. The mobility can be calculated using the following formula[13]:

$$\mu = \frac{\mathrm{d}I_{ds}}{\mathrm{d}V_{gs}} \times \frac{L}{W \times C_{ox} \times V_{ds}}, \quad (1)$$

where L and W represent the length and width of the channel (L: 5 μm and W: 4 μm), C_{ox} is the capacitance of SiO_2 with a value of 11.5 nF cm^{-2}. The electron mobility (μ_e) and hole mobility (μ_h) of the $SnS/SnSe_2$ photodetector were determined to be 45.3 and 41.2 cm^2/(V·s), respectively, while the μ_h and μ_e values of the $SnSe/SnSe_2$ photodetector were determined to be 21.5 and 18.3 cm^2/(V·s), respectively. These values were found to be considerably higher than those of the individual $SnSe_2$ (10 cm^2/(V·s)), SnS (5.29 cm^2/(V·s)), and SnSe (6.84 cm^2/(V·s)) thin layers as shown in Fig. S2.

To evaluate the photodetection performance of the $SnS/SnSe_2$ and $SnSe/SnSe_2$ photodetectors under 405 nm illumination, the semi-logarithmic current–voltage (I_{ds}–V_{ds}) curves were measured at various power densities (17.8, 35.7, 75.3 μW·mm^{-2}), as depicted in Figs. 4(a) and 4(b). The rectification behavior remained consistent as the light power density increased, with a noticeable increase in the forward current. The dark current (I_{dark}) of both heterostructure photodetectors (0.5 μA) was observed to be one order of magnitude lower than that of $SnSe_2$-based photodetectors (5.1 μA, Fig. S3).

The current–time (I_{ds}–T) curves of the $SnS/SnSe_2$ and $SnSe/SnSe_2$ photodetectors were obtained at V_{ds} = 5 V and V_{gs} = 0 V with a modulation frequency of 50 mHz, as presented in Figs. 4(c) and 4(d), respectively. An immediate response to the 405 nm light was observed, with the current increasing to saturation as soon as the laser was activated, and swiftly decaying to the initial state when the laser was turned off. After storage for three weeks, the photodetectors still exhibited stable and repeatable switching cycles, which can be attributed to the films possessing inert properties[29].

The response time, including the rise time (τ_r) and fall time (τ_f), was defined as the time of the photocurrent I_{ph} ($I_{ph} = I_{ds} - I_{dark}$) increased from 10% to 90% and decayed from 90% to 10%, respectively[30]. The rise/fall time of the $SnS/SnSe_2$ and $SnSe/SnSe_2$ photodetectors was estimated to be 3.13/4.54 ms and 4.74/5.18 ms, respectively, which is one order of magnitude less than that of the photodetector based on the $SnSe_2$ thin layers (Fig. S3), as shown in Fig. 4(e). The scatter plots of photocurrent–light power intensity are displayed in Fig. 4(f), and can be fitted using the formula[16]:

$$I_{ph} = aP^{\alpha}, \quad (2)$$

where a is a constant, P is the light power intensity, and α is the fitted parameter, reflecting the efficiency of photocurrent conversion. The α values were estimated to be 0.69 and 0.60 for the $SnS/SnSe_2$ and $SnSe/SnSe_2$ photodetector, respectively, which are larger than that of the photodetector based on the $SnSe_2$ thin layers (0.32, Fig. S4), indicating an increased photocurrent conversion efficiency. The observed α values were all less than 1, a behavior that has been widely reported in photodetectors based on 2D materials, owing to the presence of trap centers within the channel material[16].

Both the $SnS/SnSe_2$ and $SnSe/SnSe_2$ photodetectors exhibit broad-spectrum photodetection characteristics, as illustrated in Figs. 5(a) and 5(b), as well as in Fig. S5 and S6, upon illumination with wavelengths ranging from 405 to 850 nm. While the photocurrents of the two photodetectors vary under different wavelengths of illumination, their exceptional broad-spectrum photodetection abilities are evident across the near-ultraviolet to near-infrared spectrum. The pho-

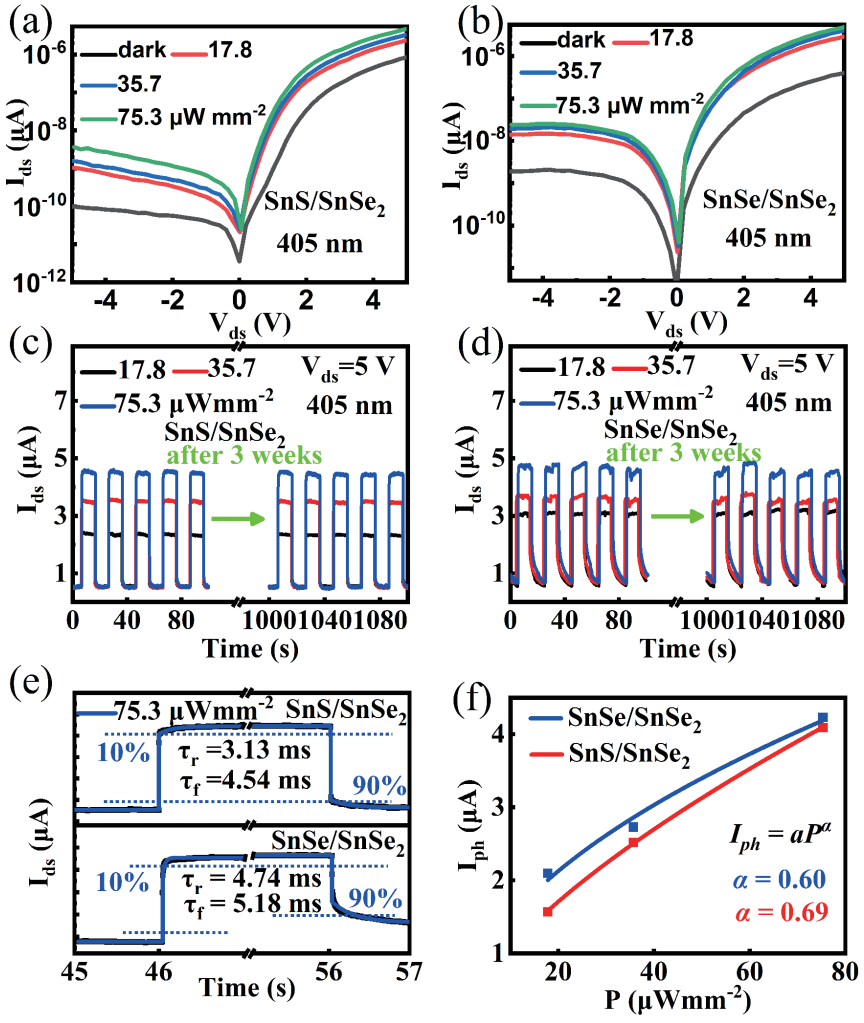

Fig. 4. (Color online) (a) and (b) The semi-logarithmic current–voltage curves of the $SnS/SnSe_2$ and $SnSe/SnSe_2$ photodetectors. (c) and (d) Transient photoresponse of the $SnS/SnSe_2$ and $SnSe/SnSe_2$ photodetectors. (e) and (f) Response time and photocurrent–power density plots of the two types of photodetectors.

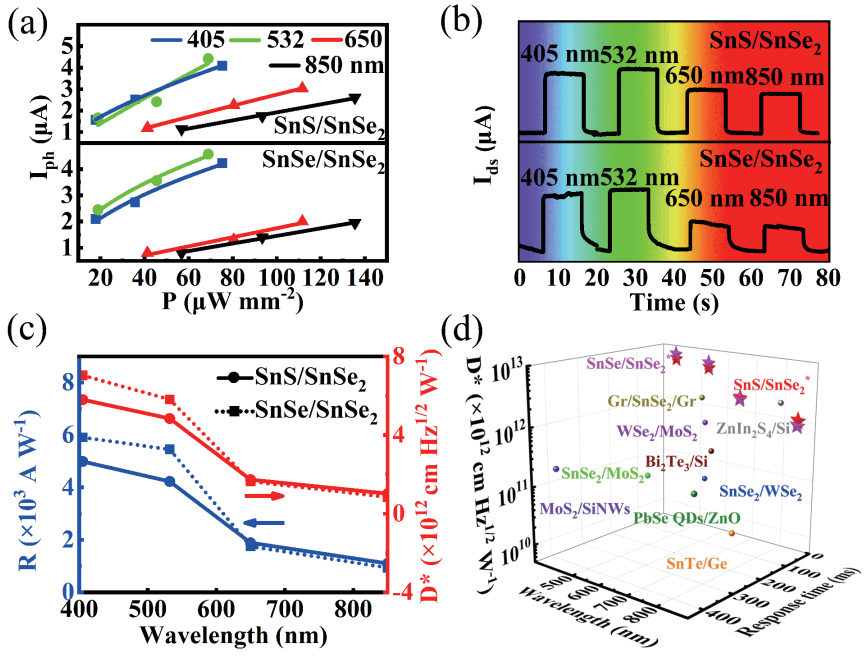

Fig. 5. (Color online) (a) Photocurrent–power density plots of the $SnS/SnSe_2$ and $SnSe/SnSe_2$ photodetectors under different wavelengths. (b) Transient photoresponse under different wavelengths. (c) Responsivity and normalized detectivity as a function of wavelength. (d) Comparison of normalized detectivity and response time of our devices with photodetectors based on other heterostructures under different wavelengths.

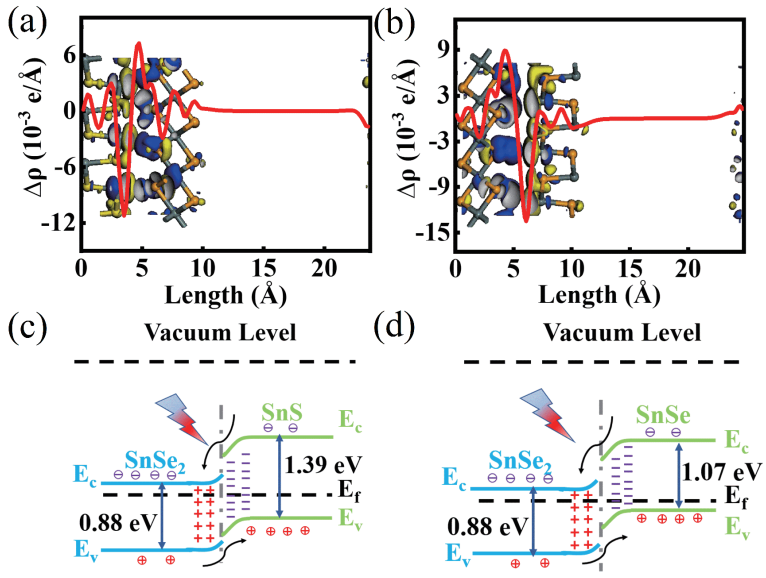

Fig. 6. (Color online) (a) and (b) Planar-averaged charge density difference of the SnS/$SnSe_2$ and SnSe/$SnSe_2$ heterostructures. (c) and (d) Band alignments of the SnS/$SnSe_2$ and SnSe/$SnSe_2$ heterostructures.

toresponsivity (R) and external quantum efficiency (EQE), two fundamental parameters for assessing a photodetector, can be derived using the following formulas[31, 32]:

$$R = \frac{I_{ph}}{PS}, \tag{3}$$

$$\mathrm{EQE} = \frac{hcR}{e\lambda}, \tag{4}$$

where λ is the incident wavelength, S is the effective area, and the size of the channel is smaller than the laser spot, therefore the effective area is 20 μm^2 (length × width: 4 × 5 μm^2)[33]. Typically, noise in photodetectors comprises flicker noise, thermal noise, and shot noise[34]. The noise current (I_N) of the SnS/$SnSe_2$ and SnSe/$SnSe_2$ photodetectors can be derived from the fast Fourier transform of the dark current (see Fig. S7)[35]. At frequencies lower than 14.7 Hz (12.5 Hz), flicker noise is the dominant noise source and demonstrates a linear relationship with frequency. At higher frequencies exceeding 14.7 Hz (12.5 Hz), the noise is composed of thermal noise ($I_T = \sqrt{\frac{4K_BT}{R_{sh}}}$) and shot noise ($I_s = \sqrt{2eI_{dark}}$). As a result, the normalized detectivity (D^*), which is indicative of the photodetector's ability to detect weak signals, is calculated using the following formula[36]:

$$D^* = \frac{R\sqrt{S}}{I_N} = \frac{R\sqrt{S}}{\sqrt{2eI_{dark} + \frac{4k_BT}{R_{sh}}}}, \tag{5}$$

where k_B is the Boltzmann constant, and R_{sh} is the resistance. Table S1 and Fig. 5(b) present the computed R and D^* values, which reveal a declining trend as the incident wavelength increases. When exposed to 405 nm light, the SnS/$SnSe_2$ and SnSe/$SnSe_2$ photodetectors exhibit maximal R values of 4.99 × 10^3 and 5.91 × 10^3 A·W^{-1}, respectively. These values are notably greater than those of photodetectors based on individual $SnSe_2$ (2.46 × 10^3 A·W^{-1}, Fig. S8), SnS (1.19 × 10^3 A·W^{-1}), and SnSe (1.37 × 10^3 A·W^{-1}). The corresponding EQE values are 1.53 × 10^4% and 1.81 × 10^4% (Fig. S9). The D^* values of the SnS/$SnSe_2$ and SnSe/$SnSe_2$ photodetectors are calculated to be 5.78 × 10^{12} and 7.03 × 10^{12} cm·$Hz^{1/2}$·W^{-1}, respectively, which are one order of magnitude greater than those of photodetectors based on individual $SnSe_2$ (8.79 × 10^{11} cm·$Hz^{1/2}$·W^{-1}, Fig. S8), SnS (5.69 × 10^{11} cm·$Hz^{1/2}$·W^{-1}), and SnSe (9.82 × 10^{11} cm·$Hz^{1/2}$·W^{-1}). It is worth noting that the SnS/$SnSe_2$ and SnSe/$SnSe_2$ photodetectors respond well to 850 nm light, demonstrating considerable photoresponsivities of 9.39 × 10^2 and 1.10 × 10^3 A·W^{-1}, as well as substantial normalized detectivities of 1.02 × 10^{12} and 8.38 × 10^{11} cm·$Hz^{1/2}$·W^{-1}.

The noise equivalent power (NEP) is an important evaluation parameter in commercial applications, which is defined as the incident light power that produces a signal equivalent to the noise level in a 1 Hz bandwidth. NEP can be calculated using the formula[37]:

$$\mathrm{NEP} = \frac{\sqrt{S}}{D^*}. \tag{6}$$

The NEP values of the SnS/$SnSe_2$ and SnSe/$SnSe_2$ photodetectors were estimated to be 8.02 × 10^{-5} and 7.29 × 10^{-5} pW·$Hz^{1/2}$, respectively. These values are notably lower by five orders of magnitude than those of conventional photodetectors (12 pW·$Hz^{1/2}$, PDB230A, Thorlabs) as depicted in Fig. S9. Hence, considering the photoresponsivity, normalized detectivity, noise equivalent power, and response time, the SnS/$SnSe_2$ and SnSe/$SnSe_2$ photodetectors demonstrate superior performance compared to photodetectors based on other heterostructures, such as WSe_2/MoS_2[38], SnTe/Ge[39], and others[16, 40–47], as demonstrated in Fig. 5(c). Furthermore, the photodetectors are comparable to, and in some cases even surpass, commercial photodetectors.

Furthermore, first-principles calculations based on density functional theory (DFT) were performed to provide additional insights into the properties of the heterostructures[48].

The detailed setting information is shown in the supplementary information. Figs. 6(a) and 6(b) depict planar-averaged and three-dimensional isosurfaces of the charge density differences for the $SnS/SnSe_2$ and $SnSe/SnSe_2$ heterostructures. The blue part signifies electron accumulation, while the yellow part represents electron depletion. The redistribution of charge density was observed at the interface of the two heterostructures, where electrons were accumulated in $SnSe_2$ but depleted in SnS and SnSe, demonstrating for the presence of the built-in electrical field. The DFT-computed band gaps of $SnSe_2$, SnS, and SnSe were determined to be 0.88, 1.39, and 1.07 eV, respectively, as illustrated in Fig. S10. The band alignments of the $SnS/SnSe_2$ and $SnSe/SnSe_2$ heterostructures were displayed in Figs. 6(c) and 6(d). Because the conduction band minimum and the valence band maximum of $SnSe_2$ were lower than those of SnS and SnSe, both the $SnS/SnSe_2$ and $SnSe/SnSe_2$ heterostructures were categorized as type–Ⅱ heterostructures.

The excellent photodetection performance of heterostructures can be attributed to the following reasons. Firstly, the built-in electric field effectively separated the photo-generated carriers, reducing their recombination rate[49]. As a result, both $SnS/SnSe_2$ and $SnSe/SnSe_2$ photodetectors demonstrated increased photocurrent and photoresponsivity. And the higher photoresponsivity of the $SnSe/SnSe_2$ photodetector than that of the $SnS/SnSe_2$ photodetector can be attributed to the higher work function difference or potential barrier. Moreover, the barrier region at the heterostructure interface prevented the majority carriers, hence decreasing the dark current[50]. Because the normalized detectivity is proportional to photoresponsivity and inversely related to the dark current, the $SnS/SnSe_2$ and $SnSe/SnSe_2$ photodetectors displayed at least an order of magnitude greater normalized detectivity than their individual components. Finally, the fast response time can be attributed to two reasons: (Ⅰ) the rapid movement of photo-generated carriers toward the electrodes, enabled by the heterostructure's band offset, and (Ⅱ) the presence of clean and atomically sharp interfaces because of the interlayer van der Waals forces, which facilitated the transportation of photo-generated carriers[51, 52].

4. Conclusion

In this work, photodetectors based on $SnS/SnSe_2$ and $SnSe/SnSe_2$ heterostructures were successfully constructed using a polydimethylsiloxane (PDMS)-assisted dry-transfer method, which exhibited remarkable performance in detecting a broad range of wavelengths from 405 to 850 nm. Compared with their individual components, the $SnS/SnSe_2$ and $SnSe/SnSe_2$ photodetectors demonstrated superior characteristics such as high photoresponsivities of 4.99×10^3 and 5.91×10^3 $A{\cdot}W^{-1}$, elevated normalized detectivities of 5.80×10^{12} and 7.03×10^{12} $cm{\cdot}Hz^{1/2}{\cdot}W^{-1}$, and faster response times of 3.13 and 4.74 ms, respectively. The $SnS/SnSe_2$ and $SnSe/SnSe_2$ heterostructures provide new platforms for the development of $SnSe_2$-based photodetectors, and are considered promising candidates for future high-performance optoelectronic devices.

Appendix A. Supplementary material

Supplementary materials to this article can be found online at https://doi.org/10.1088/1674-4926/45/3/032703.

Acknowledgements

This work was supported by the Jilin Scientific and Technological Development Program (Grant No. 20230101286JC), National Natural Science Foundation of China (Grant Nos. 61975051, 6227503, and 52002110), Hebei Provincial Department of Education Innovation Ability Training Funding Project for graduate students.

References

[1] Novoselov K S, Geim A K, Morozov S V, et al. Electric field effect in atomically thin carbon films. Science, 2004, 306, 666
[2] Lien M R, Wang N, Wu J, et al. Resonant grating-enhanced black phosphorus mid-wave infrared photodetector. Nano Lett, 2022, 22(21), 8704
[3] Zhang F, Mo Z X, Cui B C, et al. Bandgap engineering of BiIns nanowire for wide-spectrum, high-responsivity, and polarimetric-sensitive detection. Adv Funct Material, 2023, 2306077
[4] Rahman A, Kim H, Noor-A-Alam M, et al. A theoretical study on tuning band gaps of monolayer and bilayer SnS_2 and $SnSe_2$ under external stimuli. Curr Appl Phys, 2019, 19(31), 709
[5] Shafique A, Samad A, Shin Y H. Ultra low lattice thermal conductivity and high carrier mobility of monolayer SnS_2 and $SnSe_2$: A first principles study. Phys Chem Chem Phys, 2017, 19, 20677
[6] Bibin J, Kunjomana A G, Teena M. Physical vapor deposition and enhancement of optoelectronic properties of $SnSe_2$ platelets. Sci Mater Electron, 2022, 33(35), 26397
[7] Mukhokosi E P, Roul B, Krupanidhi S B, et al. Toward a fast and highly responsive $SnSe_2$-based photodiode by exploiting the mobility of the counter semiconductor. ACS Appl Mater Interfaces, 2019, 11(6), 6184
[8] Dong W, Lu C H, Luo M W, et al. Enhanced UV–Vis photodetector performance by optimizing interfacial charge transportation in the heterostructure by SnS and $SnSe_2$. J Colloid Interface Sci, 2022, 621, 374
[9] Guo C, Guo W L, Xu H A, et al. Ultrasensitive ambient-stable $SnSe_2$-based broadband photodetectors for room-temperature IR/THz energy conversion and imaging. 2D Mater, 2020, 7(3), 035026
[10] Lv S, Liu X, Li X, et al. Electrochemical peeling few-layer $SnSe_2$ for high-performance ultrafast photonics. ACS Appl Mater Interfaces, 2020, 12(38), 43049
[11] Wang R Y, Caldwell M A, Jeyasingh R G D, et al. Electronic and optical switching of solution–phase deposited $SnSe_2$ phase change memory material. J Appl Phys, 2011, 109(11), 113506
[12] Chen Z, Xiong L, Li G, et al. Wafer-scale growth of vertical-structured $SnSe_2$ nanosheets for highly sensitive, fast-response UV–vis–NIR broadband photodetectors. Adv Opt Mater, 2022, 10(5), 2102250
[13] Zhou X, Gan L, Tian W, et al. Ultrathin $SnSe_2$ flakes grown by chemical vapor deposition for high-performance photodetectors. Adv Mater, 2015, 27(48), 8035
[14] Park H, Shin G H, Lee K J, et al. Probing temperature-dependent interlayer coupling in a MoS_2/h-BN heterostructure. Nano Res, 2020, 13(2), 576
[15] Guo T T, Song X F, Wei P F, et al. High-gain MoS_2/Ta_2NiSe_5 heterojunction photodetectors with charge transfer and suppressing dark current. ACS Appl Mater Interfaces, 2022, 14(50), 56384
[16] Zhou X, Zhou N, Li C, et al. Vertical heterostructures based on $SnSe_2/MoS_2$ for high performance photodetectors. 2D Mater, 2017, 4(2), 025048
[17] Zheng Z Q, Chen P F, Lu J T, et al. Self-assembly $In_2Se_3/SnSe_2$ heterostructure array with suppressed dark current and enhanced photosensitivity for weak signal. Sci China Mater, 2020, 63(8),

1560
[18] Kawamoto H, Higashitarumizu N, Nagamura N, et al. Micrometer-scale monolayer SnS growth by physical vapor deposition. Nanoscale, 2020, 12(45), 23274
[19] Zhao S L, Wang H, Zhou Y, et al. Controlled synthesis of single-crystal SnSe nanoplates. Nano Res, 2015, 8(1), 288
[20] Arokiya Mary T, Fernandez A C, Sakthivel P, et al. A study on the role of surfactant on the layered growth of $SnSe_2$ for electrical applications. J Mater Sci Mater Electron, 2016, 27(10), 11041
[21] Lu C L, Zhang Y W, Zhang L, et al. Preparation and photoelectrochemical properties of SnS/SnSe and SnSe/SnS bilayer structures fabricated via electrodeposition. Appl Surf Sci, 2019, 484, 560
[22] Cho S H, Cho K, Park N W, et al. Multi-layer SnSe nanoflake field-effect transistors with low-resistance Au ohmic contacts. Nanoscale Res Lett, 2017, 12(1), 373
[23] Kees de Groot C H, Gurnani C, Hector A L, et al. Highly selective chemical vapor deposition of tin diselenide thin films onto patterned substrates via single source diselenoether precursors. Chem Mater, 2012, 24(22), 4442
[24] Kumar M, Patel M, Kim J, et al. Vertically aligned crystalline SnS layers-based NIR photodetector governed by pyro-phototronic effect. Mater Lett, 2018, 213, 122
[25] Saini S, Mele P, Tiwari A. Influence of the planar orientation of the substrate on thermoelectric response of SnSe thin films. J Phys Chem Solids, 2019, 129, 347
[26] Li C, Yan X A, Song X F, et al. WSe_2/MoS_2 and $MoTe_2/SnSe_2$ van der Waals heterostructure transistors with different band alignment. Nanotechnology, 2017, 28(41), 415201
[27] Sohila S, Rajalakshmi M, Ghosh C, et al. Optical and Raman scattering studies on SnS nanoparticles. J Alloy Compd, 2011, 509(19), 5843
[28] Lee Y, Um D S, Lim S, et al. Gate-tunable and programmable n-InGaAs/Black phosphorus heterojunction diodes. ACS Appl Mater Interfaces, 2019, 11(26), 23382
[29] Yao J D, Shao J M, Wang Y X, et al. Ultra-broadband and high response of the Bi_2Te_3–Si heterojunction and its application as a photodetector at room temperature in harsh working environments. Nanoscale, 2015, 29(7), 12535
[30] Tian X Y, Liu Y S. Van der waals heterojunction $ReSe_2/WSe_2$ polarization-resolved photodetector. J Semicond, 2021, 42(3), 032001
[31] Wang Y F, Li X Z, Liu P, et al. Epitaxial growth of $CsPbBr_3$/PbS single-crystal film heterostructures for photodetection. J Semicond, 2021, 42(11), 112001
[32] Zhu W K, Wei X, Yan F G, et al. Broadband polarized photodetector based on p-BP/n-ReS_2 heterojunction. J Semicond, 2019, 40(9), 092001
[33] Wang F, Zhang T, Xie R Z, et al. How to characterize figures of merit of two-dimensional photodetectors. Nat Commun, 2023, 14, 2224
[34] Gong X, Tong M H, Xia Y J, et al. High-detectivity polymer photodetectors with spectral response from 300 nm to 1450 nm. Science, 2009, 325, 1665
[35] Wang W, Zhao D, Zhang F, et al. Highly sensitive low-bandgap perovskite photodetectors with response from ultraviolet to the near-infrared region. Adv Funct Mater, 2017, 27(42), 1703953
[36] Kublitski J, Hofacker A, Boroujeni B K, et al. Reverse dark current in organic photodetectors and the major role of traps as source of noise. Nat Commun, 2021, 12, 551
[37] Pedapudi M C, Dhar J C. Ultrasensitive p-n junction UV-C photodetector based on p-Si/β-Ga_2O_3 nanowire arrays. Sens Actuat A, 2022, 344, 113673
[38] Shin G H, Park C, Lee K J, et al. Ultrasensitive phototransistor based on WSe_2-MoS_2 van der waals heterojunction. Nano Lett, 2020, 20(8), 5741
[39] Song L Y, Tang L B, Hao Q, et al. Broadband photodetector based on SnTe nanofilm/n-Ge heterostructure. Nanotechnology, 2022, 33(42), 425203
[40] Xue H, Dai Y, Kim W, et al. High photoresponsivity and broadband photodetection with a band-engineered $WSe_2/SnSe_2$ heterostructure. Nanoscale, 2019, 11(7), 3240
[41] Peng M F, Tao Y, Hong X K, et al. One-step synthesized PbSe nanocrystal inks decorated 2D MoS_2 heterostructure for high stability photodetectors with photoresponse extending to near-infrared region. J Mater Chem C, 2022, 10(6), 2236
[42] Gao W, Zheng Z Q, Li Y T, et al. High performance tin diselenide photodetectors dependent on thickness: A vertical graphene sandwiched device and interfacial mechanism. Nanoscale, 2019, 11(28), 13309
[43] Peng M F, Liu Y, Li F, et al. Room-temperature direct synthesis of PbSe quantum dot inks for high-detectivity near-infrared photodetectors. ACS Appl Mater Interfaces, 2021, 13(43), 51198
[44] Zheng Z Q, Yao J D, Li W J, et al. Fabrication of a high performance $ZnIn_2S_4$/Si heterostructure photodetector array for weak signal detection. J Mater Chem C, 2018, 6(47), 12928
[45] Yao J D, Shao J M, Wang Y X, et al. Ultra-broadband and high response of the Bi_2Te_3–Si heterojunction and its application as a photodetector at room temperature in harsh working environments. Nanoscale, 2015, 7, 12535
[46] Sharmila B, Dwivedi P. MoS_2/SiNWs heterostructure based repeatable and highly responsive photodetector. Opt Mater, 2022, 133, 112918
[47] Xu Z H, Tang L, Zhang S W, et al. 2D MoS_2/CuPc heterojunction based highly sensitive photodetectors through ultrafast charge transfer. Mater Today Phys, 2020, 15, 100273
[48] Loos P F. Exchange functionals based on finite uniform electron gases. J Chem Phys, 2017, 146(11), 114108
[49] Yuan L, Xu Z J, Li J C, et al. Broad-spectrum and ultrasensitive photodetectors based on GeSe/SnS_2 heterostructures with type-III band alignment. Appl Phys Lett, 2023, 122(24), 241106
[50] Li K Z, Zhu Y E, Zhang Y F, et al. Built-in electric field promotes photoexcitation separation and depletion of most carriers in TiO_2: C UV detectors. Nanotechnology, 2019, 30(29), 295502
[51] Varghese A, Saha D, Thakar K, et al. Near-direct bandgap WSe_2/ReS_2 type–II pn heterojunction for enhanced ultrafast photodetection and high-performance photovoltaics. Nano Lett, 2020, 20(3), 1707
[52] Nguyen T T, Patel M, Ban D K, et al. Vertically trigonal WS_2 layer embedded heterostructure for enhanced ultraviolet–visible photodetector. J Alloy Compd, 2018, 768, 143

Xinfa Zhu got his BS from Qingdao University of Science and Technology in 2021. Now he is a MS student at Hebei University of Technology under the supervision of Associate Prof. Chao Fan. His research focuses on low-dimensional electronics.

Chao Fan got his PhD degree from the Institute of Semiconductors, Chinese Academy of Sciences, in 2015. Then he joined School of Electronic and Information Engineering at Hebei University of Technology, where he is currently an associate professor and a PhD supervisor. His research interests include low-dimensional electronic systems, opt-electron devices, and radio frequency devices based on low-dimensional materials.